CHEMISTRY

Subsurface catalysis-mediated selectivity of dehydrogenation reaction

Weiting Cai[1,2]*, Rentao Mu[1,2]*, Shenjun Zha[1,2], Guodong Sun[1,2], Sai Chen[1,2], Zhi-Jian Zhao[1,2], Hao Li[1,2], Hao Tian[1,2], Yu Tang[3], Franklin (Feng) Tao[3], Liang Zeng[1,2], Jinlong Gong[1,2]†

Progress in heterogeneous catalysis is often hampered by the difficulties of constructing active architectures and understanding reaction mechanisms at the molecular level due to the structural complexity of practical catalysts, in particular for multicomponent catalysts. Although surface science experiments and theoretical simulations help understand the detailed reaction mechanisms over model systems, the direct study of the nature of nanoparticle catalysts remains a grand challenge. This paper describes a facile construction of well-defined Pt-skin catalysts modified by different 3d transition metal (3dTM) atoms in subsurface regions. However, on the catalyst containing both surface and subsurface 3dTMs, the selectivity of propane dehydrogenation decreases in the sequences of Pt ~ PtFe > PtCo > PtNi due to the easier C–C cracking on exposed Co and Ni sites. After the exposed 3dTMs were removed completely, the C_3H_6 selectivity was found to increase markedly in the row Pt < PtNi@Pt < PtCo@Pt < PtFe@Pt, which is in line with the calculated trend of d-band center shifting. The established relationship between reactivity and d-band center shifting illustrates the role of subsurface catalysis in dehydrogenation reaction.

INTRODUCTION

Owing to their superior activity, better structural stability, and higher selectivity, bimetallic catalysts are widely used in a variety of heterogeneous catalytic processes (*1*). For example, Pt-based bimetallic catalysts show superior performance in automobile catalytic converters, in fuel cells for oxygen reduction reaction (ORR), and in the petroleum industry to catalyze a number of separated processes including, on purpose C_3H_6 production via propane dehydrogenation (PDH) (*2*). In general, the addition of another component can not only reduce noble metal consumption but also often tune the catalytic properties of catalysts (*3*, *4*).

For bimetallic catalytic systems, the most frequently studied structures include core-shell, alloy, and sandwich-like arrangements (*5*). For example, under a working condition of acid solution, the Pt-skin structure was formed on PtFe, PtCo, and PtNi bimetallic catalysts, which showed better ORR performance than pure Pt (*6*–*10*). Similarly, structural Ru@Pt core-shell nanoparticles also show better CO oxidation reactivity than pure Pt and PtRu alloyed catalysts (*11*, *12*). Moreover, a sandwich-like (NiO_{1-x}/Pt/Ni/Pt) catalyst consisting of both surface Ni and subsurface Ni atoms presents remarkable CO oxidation reactivity. One of the main reasons is that the subsurface Ni lowers the reaction barrier of CO + O→CO_2 on Pt (*5*). Theoretical calculations have pointed out that the d-band center of the surface Pt would be downshift-induced by TMs in subsurface regions, which consequently weakens the adsorption of adsorbates on the Pt surface (*13*). In addition to the catalytic role of subsurface metal atoms, the population of subsurface C and H also strongly influences the surface reactions and plays a major role in the selectivity of palladium-catalyzed alkyne hydrogenation (*14*–*16*). Moreover, subsurface O species in Ag catalysts are essential for the epoxidation of ethene due to the electronic effect of the subsurface O on the surface-adsorbed reactant O (*16*). Hence, understanding the catalytic role of subsurface metal atoms and nonmetal species is of great importance in heterogeneous catalysis.

Pt-based bimetallic catalysts are also extensively used in PDH because of their excellent activity and stability (*17*–*20*). Since shale gas has become an increasingly important source of propane, C_3H_6 production via PDH has attracted tremendous interest in a broad range of scientific and technological processes (*17*, *18*). However, as an endothermic process, PDH requires operation at high temperatures, which results in hydrocarbon cracking and restriction of the C_3H_6 selectivity (*17*, *18*). To improve the PDH reactivity of Pt-based catalysts, metal promoters, such as Sn, Cu, and Zn, have often been added (*18*). For example, PtCu alloyed nanoparticles supported on Al_2O_3 show higher conversion and C_3H_6 selectivity, which has been attributed to the increased Pt dispersion and electron transfer from Cu to Pt (*18*). But the exact surface structure of PtCu bimetallic catalysts is unclear. For PtSn/Al_2O_3 catalysts, although a number of works have established their superior reactivity, the active structure, in particular the chemical state of Sn, is still a subject of continuing debate (*20*, *21*). The difficulties mainly stem from the uncertainty of the preparation processes and the structural complexity of supported nanoparticles, so the exact structure of Pt-based bimetallic catalysts and reaction mechanisms in PDH processes remain somewhat controversial (*20*).

This paper describes a facile construction of Pt-3dTM [3dTM (3d transition metal) = Fe, Co, and Ni] bimetallic catalysts and explores the influence of surface 3dTMs and subsurface 3dTMs for the PDH reaction. Experimental evidence indicates that the 3dTMs in subsurface regions significantly promote the C_3H_6 selectivity compared with monometallic Pt catalyst. In contrast, the surface 3dTMs decrease the C_3H_6 selectivity because of the easier C–C cracking on exposed 3dTM sites. Combined with density functional theory (DFT) calculations, the reaction mechanism of PDH on Pt-skin surfaces modified by different subsurface 3dTM atoms (Pt-3dTM@Pt) is further revealed.

RESULTS

Structural characterization

We prepared Pt-3dTM bimetallic catalysts by a wetness coimpregnation method combined with post–acid leaching treatments. Note that

[1]Key Laboratory for Green Chemical Technology of Ministry of Education, School of Chemical Engineering and Technology, Tianjin University, Tianjin 300072, China. [2]Collaborative Innovation Center of Chemical Science and Engineering, Tianjin 300072, China. [3]Departments of Chemical and Petroleum Engineering and Chemistry, University of Kansas, Lawrence, KS 66045, USA.
*These authors contributed equally to this work.
†Corresponding author. Email: jlgong@tju.edu.cn

SBA-15 was selected as a support because the industrially used Al_2O_3 material would be dissolved in acid leaching treatment (HNO_3 solution). In addition, SBA-15 has stable and well-ordered mesoporous structures, which provide confined nanospace for many nanoparticle catalysts (*22*). Figure 1 (A and B) presents transmission electron microscopy (TEM) images of PtFe@Pt/SiO_2 and PtFe@Pt/SBA-15 catalysts, respectively. Statistical analysis for ~200 nanoparticles shows that the average size of a PtFe@Pt/SBA-15 catalyst is 6.9 ± 0.5 nm, whereas the average size of a PtFe@Pt/SiO_2 catalyst is 21.4 ± 1.9 nm, indicating that the mesoporous structure of SBA-15 can prevent the nanoparticles inside from severe agglomeration after the reduction in H_2 at 600°C. Furthermore, the size distribution of PtFe@Pt/SBA-15 is more uniform than the size distribution of PtFe@Pt/SiO_2 (insets in Fig. 1, A and B), which also indicates that most of the PtFe@Pt nanoparticles are confined in the mesopores of SBA-15.

Because Pt precursors can be more easily reduced to metallic nanoparticles than 3dTM precursors, the initial structure of Pt-3dTM catalysts after the reduction should be Pt nanoparticles decorated by 3dTM species on surface (*10*). As the reducing temperature increases, 3dTM atoms on the surface start to diffuse into the subsurface regions of Pt crystals (*5*, *7*, *10*). Acid leaching of prereduced Pt-3dTM catalysts can remove the surface 3dTM atoms, while those in subsurface regions remain unchanged because of the protection of a Pt shell, thus producing a Pt-skin or Pt-skeleton surface with 3dTM atoms in subsurface regions (*10*, *23*). To study the surface structure of leached catalysts, we measured the concentrations of Fe and Pt in acid solutions by inductively coupled plasma atomic emission spectrometry (ICP-AES). For the PtFe/SBA-15 sample reduced at 600°C, Fig. 1C shows the Fe and Pt concentrations as a function of leaching time. As a reference, the freshly prepared PtFe/SBA-15 catalyst without reduction is also treated by the leaching process. For this sample, the relative concentrations of Fe and Pt are set to 100% (*24*). After acid leaching treatment for 5 min, ~14% of Fe from prereduced PtFe/SBA-15 was found in solution, while only a negligible amount of Pt was detected. As the leaching time increases to 10 min, ~25% of Fe was leached away, and this percentage remains almost constant over an extended period of leaching time. Accordingly, we propose that surface Fe atoms should be removed completely after 10 min of leaching treatment, leaving ~75% of Fe in subsurface regions. Also note that ~5% of Pt is detected after leaching treatment with extended time, which can be attributed to the detachment of PtFe nanoparticles induced by long-time ultrasonic treatment.

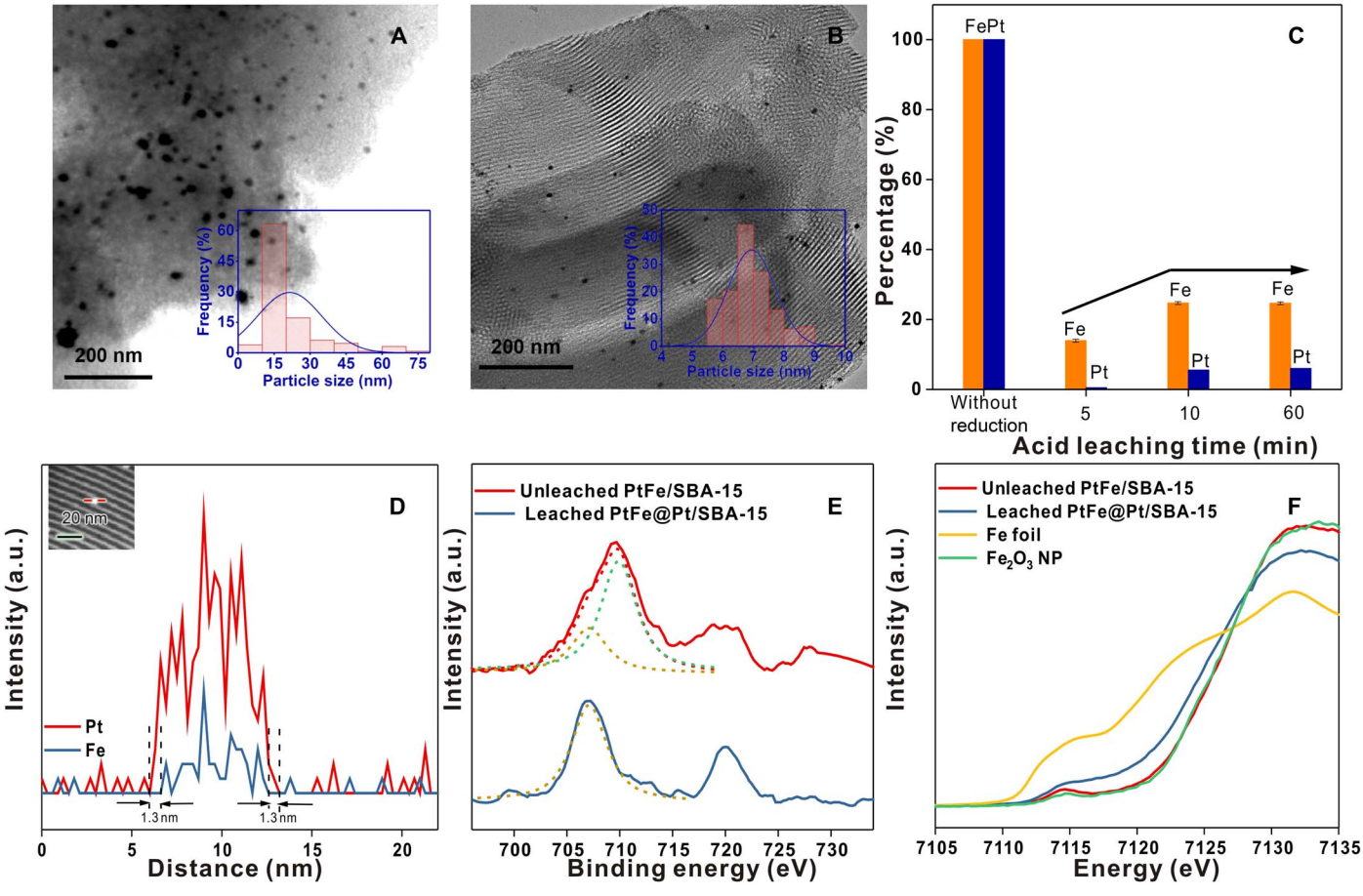

Fig. 1. Structural characterization of the Pt and PtFe nanoparticle catalysts. TEM images of leached (**A**) PtFe@Pt/SiO_2 and (**B**) PtFe@Pt/SBA-15 via same reduction treatment. The insets in (A) and (B) show the size distribution of PtFe@Pt/SiO_2 and PtFe@Pt/SBA-15, respectively. (**C**) Concentration of Fe and Pt in acid solution as a function of leaching time. The values from the unreduced sample are included as a reference. (**D**) EDS line profiles of leached PtFe@Pt/SBA-15 (inset of the nanoparticle). a.u., arbitrary units. (**E**) XPS Fe2p peaks from unleached PtFe/SBA-15 and leached PtFe@Pt/SBA-15 catalysts after air exposure at room temperature. (**F**) XANES Fe K-edge structures from PtFe/SBA-15 and PtFe@Pt/SBA-15 catalysts after air exposure at room temperature. Standard Fe foil and Fe_2O_3 samples are included as references. NP, nanoparticle.

Figure S1A shows the x-ray diffraction (XRD) patterns of the Pt/SBA-15 and PtFe@Pt/SBA-15 catalysts. For Pt/SBA-15, the 2θ peak is found at 39.7°, corresponding to the (111) plane of pure Pt crystals (*4*). However, the 2θ peak of PtFe@Pt/SBA-15 shifts to 39.9°, which should be from the PtFe alloy phase (*25*). Simultaneously, the lattice spacing of Pt/SBA-15 (d = 0.225 nm) is larger than that of PtFe@Pt/SBA-15 (d = 0.215 nm) (fig. S1, B and C), which also represents the formation of PtFe alloy in PtFe@Pt/SBA-15, in good agreement with XRD results. In addition, to confirm the formation of the Pt-skin structure with Fe in subsurface regions, Fig. 1D presents the energy-dispersive spectroscopy (EDS) line profiles of PtFe@Pt catalysts. From the EDS line profiles of Pt and Fe, the thickness of the Pt shell is determined to be ~1.3 nm. For comparison, the EDS line profiles of the PtFe/SBA-15 sample before acid leaching are also included (fig. S2), where Fe can be found on surface.

Air exposure may induce the oxidation of 3dTMs on the surface, while 3dTMs in subsurface regions do not change chemical states (*5*, *10*). Therefore, x-ray photoelectron spectroscopy (XPS) investigation was used to study the surface structures. As shown in Fig. 1E, after air exposure at room temperature, the main peak of $Fe2p_{3/2}$ for leached PtFe@Pt/SBA-15 is located at 707.9 eV, which has been assigned to metallic Fe (*26*). However, the width of the $Fe2p_{3/2}$ peak for unleached PtFe/SBA-15 is much larger than that for the leached sample. Deconvolution of the $Fe2p_{3/2}$ peak for the unleached sample yields two peaks located at 707.9 and 709.9 eV, corresponding to Fe^0 and

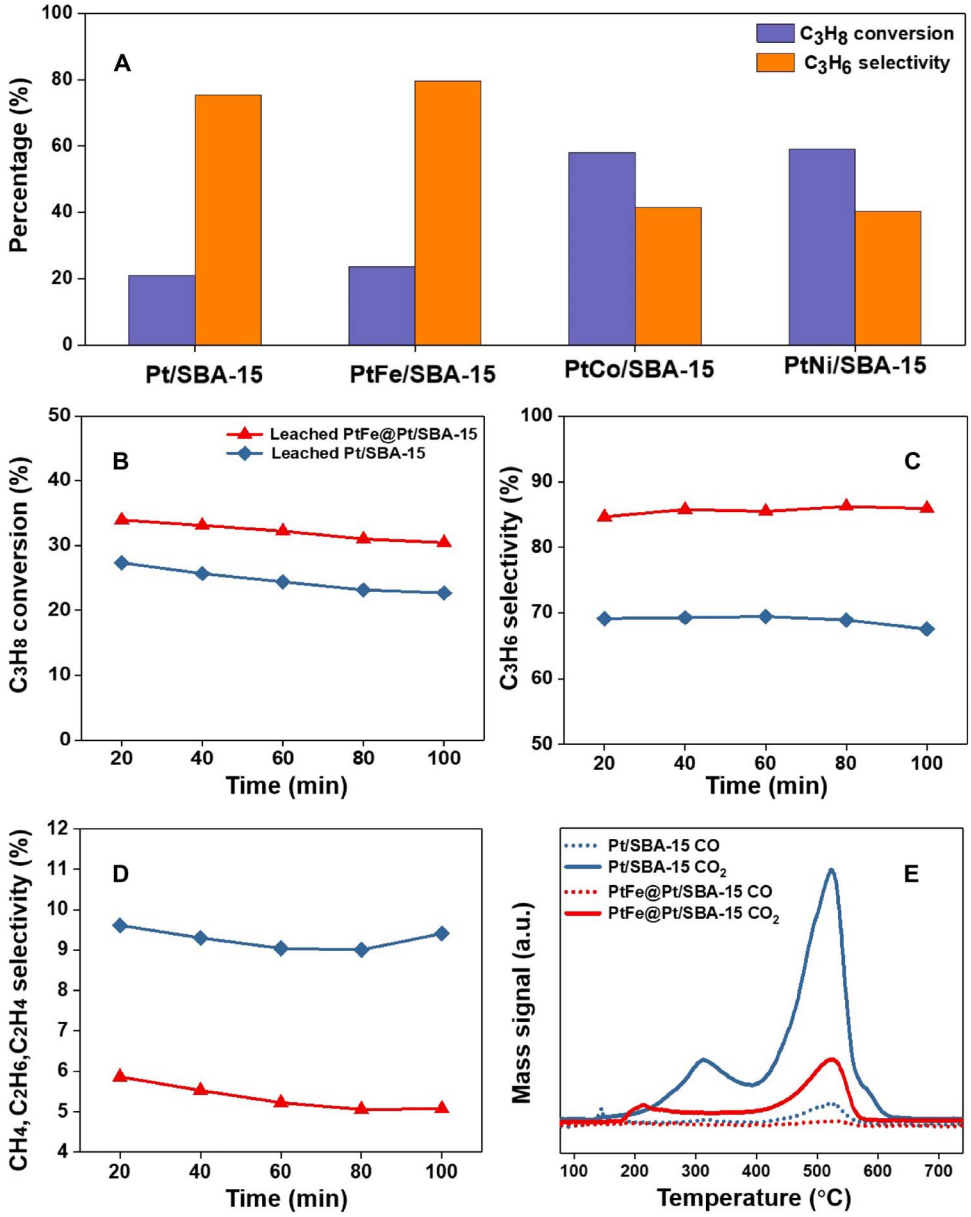

Fig. 2. Catalytic performance in PDH. (**A**) C_3H_6 selectivity and C_3H_8 conversion over different unleached Pt-3dTM/SBA-15 catalysts. (**B**) C_3H_8 conversion and (**C**) C_3H_6 selectivity over leached PtFe@Pt/SBA-15 and Pt/SBA-15 catalysts. (**D**) Summed selectivity of CH_4, C_2H_6, and C_2H_4 by-products as a function of reaction time. (**E**) TPO profiles of spent Pt/SBA-15 and PtFe@Pt/SBA-15 catalysts.

Fe^{3+} species, respectively (*27*). Note that Pt maintains a metallic state on leached and unleached samples when exposed to air at room temperature (fig. S3). XPS results illustrate that, before acid leaching, Fe locates not only on the surface but also in subsurface regions. The surface Fe becomes oxidized when exposed to air, while the Fe in subsurface regions keeps a metallic state in air due to the kinetic limit of outward diffusion of Fe (*5*). After acid leaching, surface Fe can be removed completely. The remaining Fe in subsurface regions does not change its chemical state when exposed to air at room temperature.

Further, we carried out x-ray absorption near-edge structure (XANES) measurements to study the chemical state of Fe in the PtFe/SBA-15 before and after acid leaching. Figure 1F exhibits the Fe K-edge XANES spectra acquired from these samples. In comparison, we also included the spectra recorded from Fe_2O_3 nanoparticles and standard metallic Fe foil as references. It has been proposed that the adsorption energies at 7115 and 7132 eV represent an electronic transition from 1s to 3d orbitals and a 1s-to-4p transition in Fe atoms, respectively (*28*). Before acid leaching, the Fe K-edge structure resembles that of Fe_2O_3, with the high intensity of the white line caused by the Fe-O interaction (*29*). Inversely, after acid leaching, the intensity of the white line decreases; moreover, the position of the pre-edge feature shifts to lower energy, and the spectra become similar to that of metallic Fe foil. The Fe K-edge XANES study demonstrates that the chemical state of Fe changes from an oxidized state to a metallic state after acid leaching when exposed in air. XANES studies further support the formation of Pt-skin structure with inner metallic Fe, which is consistent with the ICP and XPS results.

To prepare PtCo@Pt/SBA-15 and PtNi@Pt/SBA-15 catalysts, we conducted the same prereduction combined with acid leaching procedure. Therefore, the similar Pt-skin structure with inner Co or Ni atoms should be synthesized.

Catalytic performance

The reactivity to PDH (C_3H_8, 7 ml/min; H_2, 7 ml/min; N_2, 11 ml/min) was studied over different Pt-3dTM/SBA-15 catalysts. For comparison, the reactivity of Pt/SBA-15 was also tested. First, Fig. 2A displays the PDH reactivity of unleached Pt-3dTM/SBA-15 and Pt/SBA-15 catalysts. The unleached PtFe/SBA-15 catalyst, containing both surface and subsurface Fe, shows a reactivity comparable to that of Pt/SBA-15, where the C_3H_8 conversion and C_3H_6 selectivity are found to be ~21 and ~75%, respectively. On PtCo/SBA-15 and PtNi/SBA-15 catalysts, the C_3H_8 conversion increases with 37 and 38% compared to that on Pt/SBA-15. But the C_3H_6 selectivity decreases to 41 and 40%, respectively. As expected, the lower selectivity on unleached Pt-3dTM/SBA-15 catalysts can be attributed to the high C–C cracking capability of Co and Ni sites on the surface (*30*).

After the removal of surface Fe atoms, the C_3H_8 conversion of the PtFe@Pt/SBA-15 catalyst becomes ~10% higher than that of the Pt/SBA-15 catalyst. Since the size distribution of PtFe@Pt/SBA-15 is similar to that of Pt/SBA-15, more nanoparticles, with more exposed metal atoms, can be obtained through Fe addition, thus leading to higher propane conversion. Note that, since the catalysts are confined in the mesoporous structure of SBA-15, C_3H_8 conversion decreased slightly in 100 min of reaction time (Fig. 2B), which is much more stable than the Pt-based catalysts supported on Al_2O_3 (*17*, *19*). As shown in Fig. 2C, the C_3H_6 selectivity of the leached PtFe@Pt/SBA-15 catalyst is ~15% higher than that of the Pt/SBA-15 catalyst. Given that PtFe@Pt/SBA-15 presents a similar pure Pt surface and size distribution as Pt/SBA-15, the improved C_3H_6 selectivity over PtFe@Pt/SBA-15 can be attributed to the promotion of Fe in subsurface regions.

Figure 2D further displays the summed selectivity of CH_4, C_2H_4, and C_2H_6 as a function of reaction time. On the Pt/SBA-15 catalyst, the summed selectivity of gaseous by-products is about 9.6%, while on the PtFe@Pt/SBA-15 catalyst, the summed selectivity of gaseous by-products is suppressed to 5 to 6%. Upon deep C–H breaking, coke would form, which may block active sites and decrease C_3H_6 selectivity (*19*). To evaluate the amount of coke, we performed temperature-programmed oxidation (TPO) measurements in Fig. 2E. For the spent Pt/SBA-15 catalyst, we found two peaks of CO and CO_2 at ~300° and ~500°C, respectively. The peak at a lower temperature can be attributed to the oxidation of coke deposited on metal sites, while that at a higher temperature should be related to coke on support (*31*). On the other hand, we found that the peak intensities of CO and CO_2 from PtFe@Pt/SBA-15 are much lower than those from Pt/SBA-15, indicating that Fe atoms in subsurface regions suppress coke formation. TPO experiments were also conducted for spent PtCo@Pt/SBA-15 and PtNi@Pt/SBA-15 catalysts (fig. S4). Similarly, subsurface Co and Ni atoms suppress the coke formation in PDH. The summed selectivity of gaseous by-products and TPO analysis agree with the higher C_3H_6 selectivity on Pt-skin catalysts modified by 3dTM atoms in subsurface regions.

DFT calculations

DFT calculations provide further insight into the effect of subsurface 3dTM atoms on PDH. As shown in table S1, the d-band center of surface Pt is found to downshift from −1.96 to −2.38, −2.29, and −2.16 eV when adding Fe, Co, and Ni into the subsurface regions, respectively. As a result, the adsorption energy of C_3H_6 decreases from −1.47 eV on a pure Pt (111) surface to −0.60, −0.68, and −0.86 eV on PtFe@Pt, PtCo@Pt, and PtNi@Pt, respectively. Previous experimental and theoretical studies have shown a similar phenomenon, where 3dTM atoms in subsurface regions weaken the interaction of small molecules (CO, O_2, and H_2) with a Pt-skin surface (*13*). In agreement with DFT results, the temperature-programmed desorption (TPD) studies show that the desorption temperature of C_3H_6 shifts to lower temperatures when Fe is in subsurface regions (fig. S5). Furthermore, Fig. 3 plots

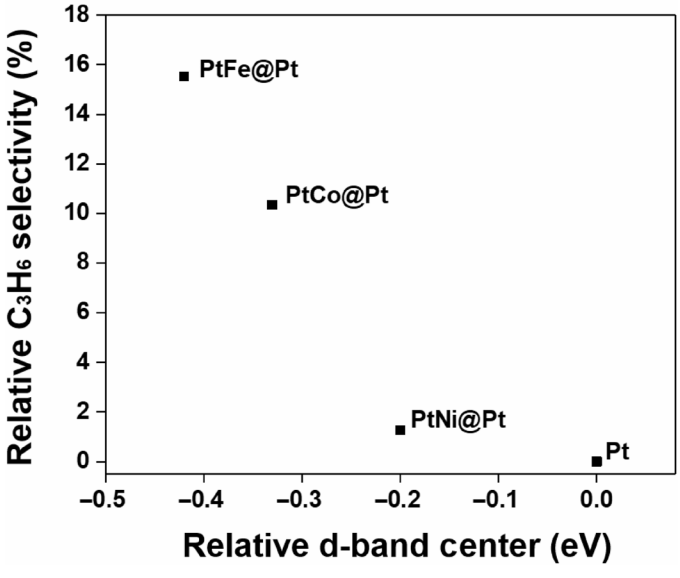

Fig. 3. Relationship between C_3H_6 selectivity and d-band center shifting. Relationship between experimental C_3H_6 selectivity and calculated d-band center positions over different catalysts.

the dependence of experimental C_3H_6 selectivity on theoretical d-band center shifting. Opposite to the correlation between adsorption energies of C_3H_6 and d-band center shifting, the C_3H_6 selectivity increases as the d-band center downshifts in a row Pt < PtNi@Pt < PtCo@Pt < PtFe@Pt (Fig. 3 and fig. S6).

The calculated potential energy landscape for PDH processes on Pt and Pt-3dTM@Pt surfaces is shown in Fig. 4. We computed the corresponding energies of different species, with the gaseous C_3H_8 as the reference point, considering van der Waals interactions between molecules while maintaining an accurate binding energy. We found the molecularly bound C_3H_8 to have an adsorption energy of −0.24 eV on a pure Pt surface, which is comparable to those on different Pt-3dTM@Pt surfaces. Figure 4 also includes the energy barriers for

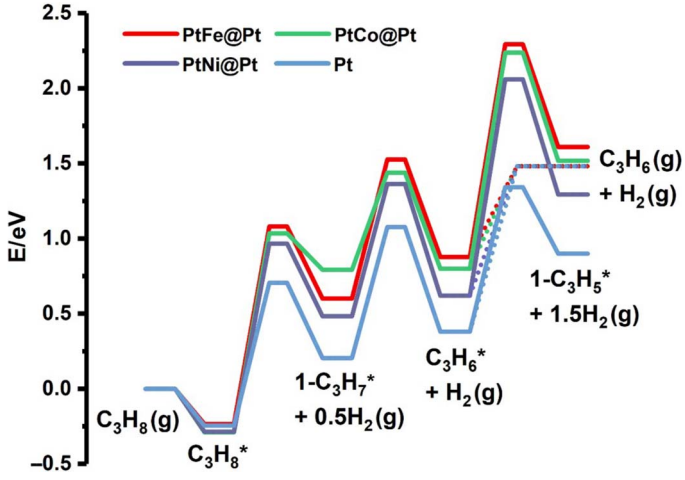

Fig. 4. Calculated energy barriers for PDH. Energy barriers for dehydrogenation steps of propane on Pt and Pt-3dTM@Pt. The dotted lines indicate the desorption barrier of C_3H_6* to gaseous C_3H_6.

PDH elementary steps. The dehydrogenation barriers of first two steps, C_3H_8*→1-C_3H_7* + 0.5H_2(g) and 1-C_3H_7*→C_3H_6* + H_2(g) on pure Pt, are 0.95 and 0.87 eV, respectively. Adding 3dTM atoms in subsurface regions results in higher barriers for dehydrogenation steps. For example, the energy barrier of the first dehydrogenation step on PtFe@Pt is 0.37 eV higher than that on Pt, and a similar trend is found for the second dehydrogenation step to produce C_3H_6* (Fig. 4). Subsequently, the competition between C_3H_6* desorption and deep C–H bond breaking will directly influence the C_3H_6 selectivity (*19*). On pure Pt, we determined the desorption energy of C_3H_6 to be 1.10 eV. However, we found the C_3H_6* feature to have a barrier energy of 0.96 eV for C–H bond breaking, indicating that the deep dehydrogenation reaction of C_3H_6 is more favorable than the desorption of C_3H_6. On the contrary, the desorption energy of C_3H_6* is lower than the energy barrier of C–H breaking of C_3H_6* on the Pt-skin surface with 3dTMs in subsurface regions. The desorption energies of C_3H_6* are 0.82, 0.76, and 0.58 eV lower than barrier energies of C–H breaking on PtFe@Pt, PtCo@Pt, and PtNi@Pt, respectively. Therefore, Pt-skin catalysts with subsurface 3dTMs present higher C_3H_6 selectivity than pure Pt catalysts. In addition to the promotion effect of subsurface 3dTMs on PDH, Pt-skin surfaces with the d-band moving away from the Fermi level can decrease the desorption energies of ethene and butene as well (*32*). Moreover, the weaker adsorption of alkene molecules often increases the activation barrier for deep dehydrogenation. As a result, Pt-skin catalysts with subsurface 3dTMs may present similar promotion effects on other dehydrogenation reactions, such as ethane and butane dehydrogenation.

DISCUSSION

For the preparation of practical catalysts used in chemical industry, the pretreatments are often necessary, such as sintering in air and activation in reducing atmospheres. However, the surface structure of catalysts achieved through these routes is complex, in particular for multicomponent catalysts, because the mass transfer may induce surface

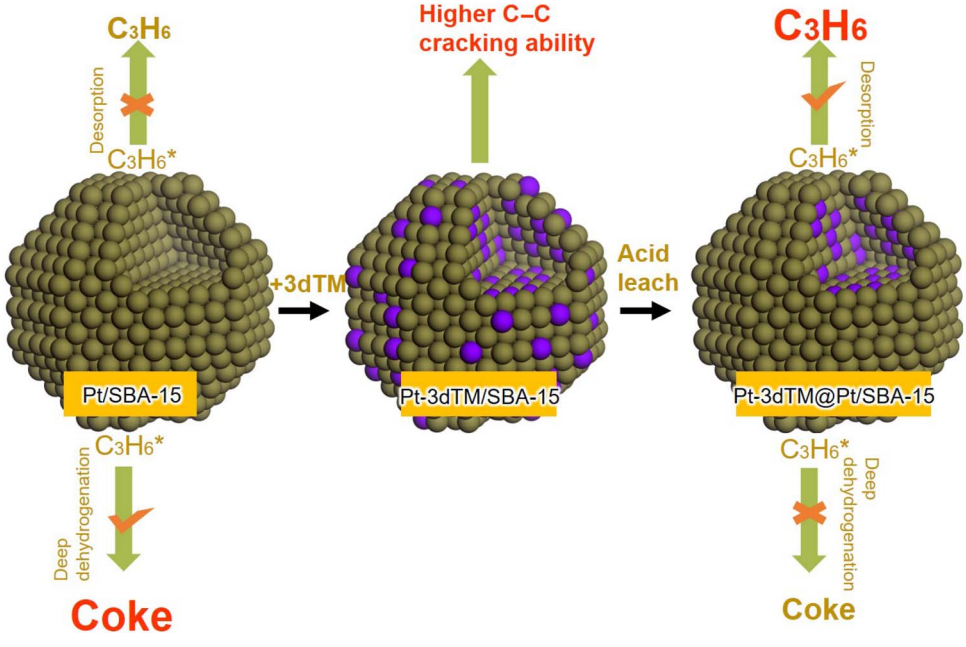

Scheme 1. Model structures. Reasonable design of efficient Pt-3dTM@Pt catalysts for PDH reaction.

reconstruction at elevated temperatures. Although the structural complexity makes the direct studies of multicomponent catalysts very challenging, a simple but effectively prepared procedure applied in our work helps construct highly efficient catalysts for dehydrogenation reactions and understand reaction mechanisms at the microscopic scale.

Here, we have systematically investigated the subsurface catalysis of 3dTM atoms and demonstrated the correlation between catalytic reactivity of dehydrogenation reactions and electronic properties. As illustrated in Schema 1, the highest C_3H_6 selectivity was observed on Pt-skin catalysts with 3dTM atoms in subsurface regions, whereas deep dehydrogenation occurs more easily on pure Pt and exposed 3dTM sites. As the d-band center downshifts, the C_3H_6 selectivity increases in the order Pt < PtNi@Pt < PtCo@Pt < PeFe@Pt, which is well consistent with the downshifting trend of the d-band center. These findings provide a promising route to prepare efficient Pt-based bimetallic catalysts for dehydrogenation reactions. We also expect that the subsurface catalysis mechanism may be widely applied in other multicomponent catalytic systems.

MATERIALS AND METHODS

Preparation of catalysts

The Pt-3dTM@Pt/SBA-15 catalysts were prepared by the wetness coimpregnation method using $H_2PtCl_6{\cdot}6H_2O$ (99.5%; Chemart), $Fe(NO_3)_3{\cdot}9H_2O$ (98.5%; Reagent), $Co(NO_3)_2{\cdot}6H_2O$ (98.5%; Kermel), and $Ni(NO_3)_2{\cdot}6H_2O$ (98%; Kermel) as precursors. The loading of Pt was controlled at 0.75 weight % (molar ratio of Pt/3dTM, 3:1). For the preparation of PtFe@Pt/SBA-15 catalysts, $H_2PtCl_6{\cdot}6H_2O$ and $Fe(NO_3)_3{\cdot}9H_2O$ were dissolved in deionized water and ethyl alcohol solution. The SBA-15 was added to the liquid solution and then stirred at room temperature for 24 hours. Then, the catalysts were dried at 60°C overnight and calcined at 300°C for 2 hours. The freshly prepared catalysts were reduced in 5% H_2/N_2 (30 ml/min) at 400°C for 4 hours. Then, 30 mg of reduced catalysts was washed in 15 ml of dilute acid solution (HNO_3 concentration, 5×10^{-4} M) for various times and dried at 60°C overnight. The concentration of Pt and Fe ions in the dilute acid solution was analyzed by ICP-AES (7700×, Agilent). TEM images were recorded using a JEM-2100F transmission electron microscope at 200 kV. The surface structure of Pt-3dTM/SBA-15 bimetallic catalysts was investigated by XRD (RigakuC/max-2500 λ = 1.5406 Å), XPS (PerkinElmer PHI 1600 ESCA), and Fe K-edge XANES measurements in the beamline BL36XU of SPring-8. TPD and TPO experiments were performed on a Micromeritics AutoChem 2920 apparatus. For C_3H_6-TPD, 100 mg of catalysts was reduced with 10% H_2/Ar at 600°C for 1 hour, and then, C_3H_6 (99.5%) was adsorbed at 100°C for 0.5 hours. The temperature was ramped up to 500°C with a heating rate of 10°C/min. The C_3H_6 desorption profiles were measured with a thermal conductivity detector. For TPO measurements, the spent catalysts (100 mg) were pretreated at 200°C for 1 hour under flowing Ar (30 ml/min) and then cooled to 50°C. Subsequently, a flow rate of 30 ml/min of 10% O_2/He with a heating rate of 10°C/min was introduced. Gas compositions were analyzed by a HIDEN QIC-20 mass spectrometer.

Reactivity test

The PDH reaction was carried out in a quartz fixed-bed reactor with an 8-mm inner diameter and a 24-cm length at the atmospheric pressure and 600°C. The reaction gas consisted of C_3H_8 (26 volume %) and H_2 (26 volume %) with N_2 as balance at a total flow of 50 ml/min. The weight hourly space velocity of propane was 3.43 g C_3H_8/(hour·g catalyst). After pelleting the catalysts to a 20– to 40–mesh size distribution, 0.24 mg of catalysts and 0.1 ml of quartz sand were loaded into the quartz tubular reactor. Before the reactivity test, each catalyst was exposed to 10 volume % H_2/N_2 at 600°C for 1 hour. The product gas was analyzed by an online gas chromatograph equipped with a flame ionization detector (Chromosorb 102 column) and a thermal conductivity detector (Al_2O_3 Plot column).

The conversion of propane was determined from Eq. 1, and the selectivity of different products was determined from Eqs. 2 to 5, respectively

$$\text{Conv}\ (\%) = \frac{[F_{C_3H_8}]_{in} - [F_{C_3H_8}]_{out}}{[F_{C_3H_8}]_{in}} \times 100 \quad (1)$$

$$\text{Sel}_{C_3H_6}(\%) = \frac{[F_{C_3H_6}]_{out}}{[F_{C_3H_8}]_{in} - [F_{C_3H_8}]_{out}} \times 100 \quad (2)$$

$$\text{Sel}_{CH_4}(\%) = \frac{[F_{CH_4}]_{out}}{3 \times ([F_{C_3H_8}]_{in} - [F_{C_3H_8}]_{out})} \times 100 \quad (3)$$

$$\text{Sel}_{C_2H_6}(\%) = \frac{[F_{C_2H_6}]_{out}}{\frac{3}{2} \times ([F_{C_3H_8}]_{in} - [F_{C_3H_8}]_{out})} \times 100 \quad (4)$$

$$\text{Sel}_{C_2H_4}(\%) = \frac{[F_{C_2H_6}]_{out}}{\frac{3}{2} \times ([F_{C_3H_8}]_{in} - [F_{C_3H_8}]_{out})} \times 100 \quad (5)$$

where F_i is the corresponding flow rate.

Calculation method

The Vienna ab initio simulation package (VASP) was used to perform calculations with the Bayesian error estimation functional–van der Waals exchange-correlation functional (*33*, *34*). Note that this generalized-gradient approximation functional provides a quantitative description of van der Waals interactions between molecules while maintaining an accurate chemisorption energy. Valence electrons were described by using a plane-wave basis set with the cutoff energy of 400 eV. Meanwhile, core electrons were treated using projector augmented wave (*35*). The Monkhorst-Pack k-points grid (3×3 ×1) was used to sample the Brillouin zone of the surface (*36*). The electronic occupancies were determined according to the Methfessel-Paxton scheme with an energy smearing of 0.15 eV, and the total energies were evaluated by extrapolating to zero broadening. The dipole correction was included in the direction perpendicular to the slab surface. A four-layer slab with a 4×4 supercell was built, and the top two layers were relaxed. All the structures were optimized until the force on each atom was less than 0.02 eV/Å. Spin polarization was taken into consideration in all the calculations.

The transition states of the reactions were determined by either the climbing nudged elastic band method or the dimer method (*37*, *38*). The optimized structure of transition state was ensured to have only one imaginary frequency.

The adsorption energy of an adsorbate, E_{ads}, was calculated as Eq. 6

$$E_{ads} = E_{total} - E_{adsorbate} - E_{surface} \quad (6)$$

where E_{total} is the total energy of the slab with an attached adsorbate, $E_{adsorbate}$ is the total energy of a gas molecule, and $E_{surface}$ is the total energy of a relaxed clean slab.

The surface d-band center (ε_d) was computed as the first and second moments of the projected d-band density of states (*39*). It was expressed as Eq. 7

$$\varepsilon_d = \frac{\int_{-\infty}^{+\infty} \rho E dE}{\int_{-\infty}^{+\infty} \rho dE} \quad (7)$$

where ρ represents the density of states, and E is the energy of state.

SUPPLEMENTARY MATERIALS

Supplementary material for this article is available at http://advances.sciencemag.org/cgi/content/full/4/8/eaar5418/DC1

Fig. S1. XRD and TEM characterization of the Pt and PtFe nanoparticles.
Fig. S2. The EDS line profiles of unleached PtFe/SBA-15 catalyst.
Fig. S3. XPS Pt4f peaks from PtFe and PtFe@Pt catalysts.
Fig. S4. TPO profiles from spent catalysts.
Fig. S5. C_3H_6-TPD of Pt and PtFe catalysts.
Fig. S6. Relative PDH reactivity of Pt and different Pt-3dTM catalysts.
Table S1. Calculated d-band center and adsorption energies of C_3H_6.

REFERENCES AND NOTES

1. J. A. Rodriguez, D. W. Goodman, The nature of the metal-metal bond in bimetallic surfaces. *Science* **257**, 897–903 (1992).
2. J. Zhang, K. Sasaki, E. Sutter, R. R. Adzic, Stabilization of platinum oxygen-reduction electrocatalysts using gold clusters. *Science* **315**, 220–222 (2007).
3. D. A. Hansgen, D. G. Vlachos, J. G. Chen, Using first principles to predict bimetallic catalysts for the ammonia decomposition reaction. *Nat. Chem.* **2**, 484–489 (2010).
4. W. Zhu, Z. Wu, G. S. Foo, X. Gao, M. Zhou, B. Liu, G. M. Veith, P. Wu, K. L. Browning, H. N. Lee, H. Li, S. Dai, H. Zhu, Taming interfacial electronic properties of platinum nanoparticles on vacancy-abundant boron nitride nanosheets for enhanced catalysis. *Nat. Commun.* **8**, 15291 (2017).
5. R. Mu, Q. A. Fu, H. Xu, H. Zhang, Y. Huang, Z. Jiang, S. Zhang, D. Tan, X. Bao, Synergetic effect of surface and subsurface Ni species at Pt–Ni bimetallic catalysts for CO oxidation. *J. Am. Chem. Soc.* **133**, 1978–1986 (2011).
6. C. Zhang, R. Zhang, X. Li, W. Chen, PtNi nanocrystals supported on hollow carbon spheres: Enhancing the electrocatalytic performance through high-temperature annealing and electrochemical CO stripping treatments. *ACS Appl. Mater. Interfaces* **9**, 29623–29632 (2017).
7. P. Strasser, S. Koh, T. Anniyev, J. Greeley, K. More, C. Yu, Z. Liu, S. Kaya, D. Nordlund, H. Ogasawara, M. F. Toney, A. Nilsson, Lattice-strain control of the activity in dealloyed core–shell fuel cell catalysts. *Nat. Chem.* **2**, 454–460 (2010).
8. V. R. Stamenkovic, B. Fowler, B. S. Mun, G. Wang, P. N. Ross, C. A. Lucas, N. M. Markovic, Improved oxygen reduction activity on $Pt_3Ni(111)$ via increased surface site availability. *Science* **315**, 493–497 (2007).
9. X. Zhao, S. Takao, K. Higashi, T. Kaneko, G. Samjeskè, O. Sekizawa, T. Sakata, Y. Yoshida, T. Uruga, Y. Iwasawa, Simultaneous improvements in performance and durability of an octahedral $PtNi_x$/C electrocatalyst for next-generation fuel cells by continuous, compressive, and concave Pt skin layers. *ACS Catal.* **7**, 4642–4654 (2017).
10. H. Xu, Q. Fu, Y. Yao, X. Bao, Highly active Pt–Fe bicomponent catalysts for CO oxidation in the presence and absence of H_2. *Energy Environ. Sci.* **5**, 6313–6320 (2012).
11. S. Alayoglu, A. U. Nilekar, M. Mavrikakis, B. Eichhorn, Ru–Pt core–shell nanoparticles for preferential oxidation of carbon monoxide in hydrogen. *Nat. Mater.* **7**, 333–338 (2008).
12. A. U. Nilekar, S. Alayoglu, B. Eichhorn, M. Mavrikakis, Preferential CO oxidation in hydrogen: Reactivity of core–shell nanoparticles. *J. Am. Chem. Soc.* **132**, 7418–7428 (2010).
13. J. R. Kitchin, J. K. Nørskov, M. A. Barteau, J. G. Chen, Modification of the surface electronic and chemical properties of Pt(111) by subsurface 3d transition metals. *J. Chem. Phys.* **120**, 10240–10246 (2004).
14. D. Teschner, J. Borsodi, A. Wootsch, Z. Révay, M. Hävecker, A. Knop-Gericke, S. D. Jackson, R. Schlögl, The roles of subsurface carbon and hydrogen in palladium-catalyzed alkyne hydrogenation. *Science* **320**, 86–89 (2008).
15. M. Armbrüster, M. Behrens, F. Cinquini, K. Föttinger, Y. Grin, A. Haghofer, B. Klötzer, A. Knop-Gericke, H. Lorenz, A. Ota, S. Penner, J. Prinz, C. Rameshan, Z. Révay, D. Rosenthal, G. Rupprechter, P. Sautet, R. Schlögl, L. Shao, L. Szentmiklósi, D. Teschner, D. Torres, R. Wagner, R. Widmer, G. Wowsnick, How to control the selectivity of palladium-based catalysts in hydrogenation reactions: The role of subsurface chemistry. *ChemCatChem* **4**, 1048–1063 (2012).
16. M. Atkins, J. Couves, M. Hague, B. H. Sakakini, K. C. Waugh, On the role of Cs, Cl and subsurface O in promoting selectivity in Ag/α-Al_2O_3 catalysed oxidation of ethene to ethene epoxide. *J. Catal.* **235**, 103–113 (2005).
17. F. Jiang, L. Zeng, S. Li, G. Liu, S. Wang, J. Gong, Propane dehydrogenation over Pt/TiO_2–Al_2O_3 catalysts. *ACS Catal.* **5**, 438–447 (2015).
18. Z. Han, S. Li, F. Jiang, T. Wang, X. Ma, J. Gong, Propane dehydrogenation over Pt–Cu bimetallic catalysts: The nature of coke deposition and the role of copper. *Nanoscale* **6**, 10000–10008 (2014).
19. L. Nykänen, K. Honkala, Selectivity in propene dehydrogenation on Pt and Pt_3Sn surfaces from first principles. *ACS Catal.* **3**, 3026–3030 (2013).
20. A. Iglesias-Juez, A. M. Beale, K. Maaijen, T. C. Weng, P. Glatzel, B. M. Weckhuysen, A combined in situ time-resolved UV–Vis, Raman and high-energy resolution X-ray absorption spectroscopy study on the deactivation behavior of Pt and Pt–Sn propane dehydrogenation catalysts under industrial reaction conditions. *J. Catal.* **276**, 268–279 (2010).
21. H. Lieske, J. Völter, State of tin in Pt–Sn/Al_2O_3 reforming catalysts investigated by TPR and chemisorption. *J. Catal.* **90**, 96–105 (1984).
22. M. S. Kumar, D. Chen, J. C. Walmsley, A. Holmen, Dehydrogenation of propane over Pt-SBA-15: Effect of Pt particle size. *Catal. Commun.* **9**, 747–750 (2008).
23. V. R. Stamenkovic, B. S. Mun, K. J. J. Mayrhofer, P. N. Ross, N. M. Markovic, Effect of surface composition on electronic structure, stability, and electrocatalytic properties of Pt-transition metal alloys: Pt-skin versus Pt-skeleton surfaces. *J. Am. Chem. Soc.* **128**, 8813–8819 (2006).
24. R. Mu, X. Guo, Q. Fu, X. Bao, Oscillation of surface structure and reactivity of PtNi bimetallic catalysts with redox treatments at variable temperatures. *J. Phys. Chem. C* **115**, 20590–20595 (2011).
25. C. Wang, X. Sang, J. T. L. Gamier, D. P. Chen, R. R. Unocic, S. E. Skrabalak, Facet-dependent deposition of highly strained alloyed shells on intermetallic nanoparticles for enhanced electrocatalysis. *Nano Lett.* **17**, 5526–5532 (2017).
26. T. Yamashita, P. Hayes, Analysis of XPS spectra of Fe^{2+} and Fe^{3+} ions in oxide materials. *Appl. Surf. Sci.* **254**, 2441–2449 (2008).
27. P. Mills, J. L. Sullivan, A study of the core level electrons in iron and its three oxides by means of X-ray photoelectron spectroscopy. *J. Phys. D Appl. Phys.* **16**, 723–732 (1983).
28. T. E. Westre, P. Kennepohl, J. G. DeWitt, B. Hedman, K. O. Hodgson, E. I. Solomon, A multiplet analysis of Fe K-Edge 1s → 3d pre-edge features of iron complexes. *J. Am. Chem. Soc.* **119**, 6297–6314 (1997).
29. M. Kotobuki, T. Shido, M. Tada, H. Uchida, H. Yamashita, Y. Iwasawa, M. Watanabe, XAFS characterization of Pt–Fe/zeolite catalysts for preferential oxidation of CO in hydrogen fuel gases. *Catal. Lett.* **103**, 263–269 (2005).
30. X. Li, D. Li, H. Tian, L. Zeng, Z.-J. Zhao, J. Gong, Dry reforming of methane over Ni/La_2O_3 nanorod catalysts with stabilized Ni nanoparticles. *Appl. Catal. B* **202**, 683–694 (2017).
31. S. I. Sanchez, M. D. Moser, S. A. Bradley, Mechanistic study of Pt–Re/γ-Al_2O_3 catalyst deactivation by chemical imaging of carbonaceous deposits using advanced X-ray detection in scanning transmission electron microscopy. *ACS Catal.* **4**, 220–228 (2014).
32. J. G. Chen, C. A. Menning, M. B. Zellner, Monolayer bimetallic surfaces: Experimental and theoretical studies of trends in electronic and chemical properties. *Surf. Sci. Rep.* **63**, 201–254 (2008).
33. J. Wellendorff, K. T. Lundgaard, A. Møgelhøj, V. Petzold, D. D. Landis, J. K. Nørskov, T. Bligaard, K. W. Jacobsen, Density functionals for surface science: Exchange-correlation model development with Bayesian error estimation. *Phys. Rev. B* **85**, 235149–235172 (2012).
34. J. J. Mortensen, K. Kaasbjerg, S. L. Frederiksen, J. K. Nørskov, J. P. Sethna, K. W. Jacobsen, Bayesian error estimation in density-functional theory. *Phys. Rev. Lett.* **95**, 216401–216405 (2005).
35. G. Kresse, D. Joubert, From ultrasoft pseudopotentials to the projector augmented-wave method. *Phys. Rev. B* **59**, 1758–1775 (1999).
36. H. J. Monkhorst, J. D. Pack, Special points for Brillouin-zone integrations. *Phys. Rev. B* **13**, 5188–5192 (1976).
37. G. Henkelman, B. P. Uberuaga, H. Jónsson, A climbing image nudged elastic band method for finding saddle points and minimum energy paths. *J. Chem. Phys.* **113**, 9901–9904 (2000).
38. G. Henkelman, H. Jónsson, Long time scale kinetic Monte Carlo simulations without lattice approximation and predefined event table. *J. Chem. Phys.* **115**, 9657–9666 (2001).

39. G. Henkelman, H. Jónsson, A dimer method for finding saddle points on high dimensional potential surfaces using only first derivatives. *J. Chem. Phys.* **111**, 7010–7022 (1999).

Acknowledgment
Funding: This work was financially supported by the National Key Research and Development Program of China (2016YFB0600901), the National Science Foundation of China (21525626, 21603159, and 91645106), and the Program of Introducing Talents of Discipline to Universities (no. B06006). F.T. and Y.T. acknowledge financial support from Chemical Sciences, Geosciences and Biosciences Division, Office of Basic Energy Sciences, Office of Science, U.S. Department of Energy under grant no. DE-SC0014561 and the U.S. NSF Career Award under grant no. NSF-CHE-14162121. **Author contributions:** J.G. proposed the concept of this work. W.C., G.S., S.C., H.L., and H.T. conducted the experiments and data analysis. S.Z. and Z.-J.Z. calculated the theoretical results. Y.T. and F.T. carried out the x-ray absorption spectroscopy measurements. R.M. and J.G. supervised the research. W.C., Z.-J.Z., L.Z., R.M., and J.G. wrote the manuscript. All authors discussed the results and commented on the manuscript. **Competing interests:** The authors declare that they have no competing interests. **Data and materials availability:** All data needed to evaluate the conclusions in the paper are present in the paper and/or the Supplementary Materials. Additional data related to this paper may be requested from the authors.

Submitted 20 November 2017
Accepted 6 July 2018
Published 10 August 2018
10.1126/sciadv.aar5418

Citation: W. Cai, R. Mu, S. Zha, G. Sun, S. Chen, Z.-J. Zhao, H. Li, H. Tian, Y. Tang, F. (F). Tao, L. Zeng, J. Gong, Subsurface catalysis-mediated selectivity of dehydrogenation reaction. *Sci. Adv.* **4**, eaar5418 (2018).

Science Advances

Subsurface catalysis-mediated selectivity of dehydrogenation reaction

Weiting Cai, Rentao Mu, Shenjun Zha, Guodong Sun, Sai Chen, Zhi-Jian Zhao, Hao Li, Hao Tian, Yu Tang, Franklin (Feng) Tao, Liang Zeng and Jinlong Gong

Sci Adv **4** (8), eaar5418.
DOI: 10.1126/sciadv.aar5418